Air Force Institute of Technology

AFIT Scholar

12-7-2020

A Computational Investigation of the Interstitial Oxidation Thermodynamics of a Mo-Nb-Ta-W High Entropy Alloy beyond the Dilute Regime

Adib J. Samin
Air Force Institute of Technology

Recommended Citation

Samin, A. J. (2020). A computational investigation of the interstitial oxidation thermodynamics of a Mo-Nb-Ta-W high entropy alloy beyond the dilute regime. Journal of Applied Physics, 128(21), 215101. https://doi.org/10.1063/5.0028977

Adib J. Samin ✉ iD

Check for updates

View Online   Export Citation   CrossMark

A computational investigation of the interstitial oxidation thermodynamics of a Mo-Nb-Ta-W high entropy alloy beyond the dilute regime

Adib J. Samin[a]

AFFILIATIONS

Department of Engineering Physics, Air Force Institute of Technology, 2950 Hobson Way, Wright-Patterson Air Force Base, Ohio 45433, USA

[a]Author to whom correspondence should be addressed: adib.samin@afit.edu

ABSTRACT

High entropy alloys (HEAs) are promising candidates for high-temperature structural material applications. Oxidation is a major factor that must be accounted for when designing such materials and it is thus important to study the oxidation behavior of HEAs to enable the optimum design of next generation materials. In this study, the thermodynamic behavior of interstitial oxygen in a Mo-Nb-Ta-W high entropy alloy was explored beyond the dilute limit. This was accomplished by sampling configurations of the HEA and HEA-oxygen systems from an isothermal–isobaric ensemble using a series of first-principle-based Monte Carlo simulations. It was found that the interstitial oxygen had comparable stability at tetrahedral (T) sites and octahedral (O) sites. The stability of the interstitial oxygen was correlated with the composition of the surrounding local metallic environment. The O-site interstitial oxygen was further found to arrange in ordered clusters and was associated with enhanced mechanical properties as demonstrated by an increase in the bulk modulus with increasing oxygen content. Finally, the solubility of the interstitial oxygen in the alloy was found to decrease with temperature.

INTRODUCTION

High entropy alloys (HEA) were originally defined to include a mixture of five or more principal elements with near equimolar concentrations. HEAs, first introduced in 2004,[1,2] represent a significant paradigm shift from the traditional alloying approach, which consists of a base material with light alloying for improved performance.[3] There have been very few significant developments with traditional alloys over the past few decades as no new base materials had been recently discovered.[3] Furthermore, traditional alloys appear to have reached their operational limits with the emergence of new technologies. HEAs, on the other hand, are very promising for a range of applications including high-temperature structural components for the aerospace industry,[4] steam turbines,[5] and nuclear energy infrastructure including molten salt reactors,[6] fusion reactors,[7] and even cryogenics.[8,9] This is due to their superior attributes as demonstrated by improved irradiation resistance,[10,11] excellent mechanical properties, high-temperature strength, good oxidation resistance,[12,13] and outstanding corrosion resistance.[14–16]

One of the fundamental limitations in the development of new materials for high-temperature structural applications is high-temperature oxidation. Refractory metals (principally Mo, W, Ta, Re, and Ru) and their alloys possess high strength and elevated melting point temperatures but they readily oxidize in air forming non-protective volatile oxides. For instance, MoO_3 has been shown to sublime at temperatures as low as 450 °C.[17,18] While there have been numerous studies reporting on HEAs over the past decade, investigations of oxygen thermodynamics and transport kinetics in high entropy alloys are currently limited in the literature, and fundamental experimental data are still lacking.[3] Müller et al.[19] attributed the superior oxidation resistance of TaMoCrTiAl at 1000 °C in air to the formation of protective Al_2O_3, Cr_2O_3, and $CrTaO_4$ oxide layers. The authors also found the slow oxygen diffusion through the $CrTaO_4$ oxide layer to be rate limiting and that titanium (Ti) was beneficial because it supported the formation of protective $CrTaO_4$. Zhang et al.[20] studied the isothermal oxidation of $Fe_{25}Cr_{20}Ni_xNb$ (0–1.6 wt. %) and found that niobium (Nb) promoted the chromium depletion underneath the oxide/matrix

interface. The authors also concluded that the oxidation of niobium at the chromia layer/metal interface could result in the spallation of the oxide scale. Jayaraj et al.[21] performed an examination of the microstructure and oxidation of the AlNbTiZr high entropy alloy. The authors found that the formation of complex oxides of $AlNbO_4$ and Ti_2ZrO_6 led to sluggish oxidation kinetics of the HEA at 1273 K for 50 h. Butler and Chaput[22] examined the oxidation resistance of an AlNbTaTiZr refractory complex concentrated alloy (RCCA). The observed oxidation resistance at 1000 °C was attributed to an outer composite oxide layer. While this layer was morphologically continuous, it consisted of a non-continuous mixture of $NbAlO_4$, ZrO_2, $Ti_7Al_2O_{15}$, and $Ta_2Nb_4O_{15}$. In 2014, Liu et al.[23] examined the oxidation behavior of four body centered cubic HEAs. It was found that the oxidation at 1300 °C followed linear kinetic behavior and that oxidation resistance was significantly improved by adding titanium and silicon but reduced with the addition of vanadium. On the computational side, Hong et al.[24] studied the oxidation behavior of $Al_{0.3}CoCrCuFeNi$ HEA by investigating the oxygen adsorption mechanisms on different crystallographic surfaces and thermodynamic stabilities of possible oxides. The cohesive energy results suggested that Al formed the most thermodynamically stable oxide (Al_2O_3) among all the alloying elements and that (Cr_2O_3) was the second most stable oxide. The adsorption energy of oxygen to the studied surfaces was the lowest for the sites with more neighboring Cr atoms. Osei-Agyemang and Balasubramanian[25] recently explored the surface oxidation mechanism for the refractory high entropy alloy Mo-W-Ta-Ti-Zr using ab initio calculations. The authors reported the HEA surface to be highly reactive to oxygen yielding a full monolayer coverage. It was further determined that pressures as low as 10^{-9} bar were incapable of removing the adsorbed oxygen from the alloy surface at 2000 K. Ferrari and Kormann[26] studied the surface segregation in Cr-Mn-Fe-Co-Ni high entropy alloys using ab initio calculations. The authors reported very strong segregation of Cr and Mn upon exposure to O.

While the reported works in the literature are important, theoretical investigations of the oxidation mechanisms and behavior of high entropy alloys are limited. Few have reported on the oxidation behavior beyond the dilute limit as far as I can tell. Enhancing our knowledge and databases for various thermodynamic and kinetic processes involved with the oxidation of multicomponent alloys is crucial. This will ultimately enable better, more efficient material designs and improve mitigation strategies against oxidation. In this work, an $Mo_Nb_Ta_W$ alloy was selected as a representative HEA system. The behavior of $Mo_{14}Nb_{12}Ta_{13}W_{15}$-$O_x$ (with $0 < x < 9$) high entropy alloys with interstitial oxygen beyond the dilute level was studied to better understand the early stages of oxidation thermodynamics. To clarify the notation for the alloy, the system contained the $3 \times 3 \times 3$ metal bcc supercell comprising a total of 54 metal atoms: 14 Mo atoms, 12 Nb atoms, 13 Ta atoms, and 15 W atoms. In addition, a varying number of interstitial oxygen atoms x, ranging from one up to nine, was also contained in the system in the present study.

COMPUTATIONAL DETAILS

In order to sample equilibrium configurations of the alloy and the oxygen containing alloys, a series of Monte Carlo simulations were performed in the NPT ensemble at 300 K and zero pressure.

The MC simulations included at least 1600 steps for equilibration and then a production run of at least 500 steps. The energy evaluations for these MC simulations were obtained via ab initio calculations that were performed by the Vienna Ab initio Simulation Package (VASP) through a python wrapper. The ab initio calculations were performed under the Density Functional Theory (DFT) framework using a plane wave basis set and the projector-augmented wave (PAW) method[27,28] as implemented in the Vienna Ab initio Simulation Package (VASP).[29,30] The generalized gradient approximation (GGA)[31] was used for the exchange correlation functionals as parametrized by Perdew–Burke and Ernzerhof (PBE).[32] The employed PAW potentials treated the following electrons as valence states: Mo ($4p^6\ 5s^1\ 4d^5$), Nb ($4p^6\ 5s^1\ 4d^4$), Ta ($6s^2\ 5d^3$), W ($6s^2\ 5d^4$), and O ($2s^2\ 2p^4$). The 5p states were not explicitly treated as valence states since these states are rather strongly localized as the 4f shell becomes filled.[33] Methfessel Paxton smearing[34] with a small broadening width of 0.1 eV was employed in all simulations. The wave functions were expanded in a plane wave basis with cutoff energies of 360 eV. The Brillouin zone was sampled by a Γ-centered $2 \times 2 \times 2$ Monkhorst–Pack grid.[35] The positions of the atoms as well as the volume and shape of the supercell were fully relaxed until the total stress became zero. In the course of the MC simulation, the self-consistent calculations converged to an accuracy of 10^{-5} eV and the atomic relaxation steps (of positions and shape/size of the supercell) were allowed to continue until the force on each atom of the system satisfied a threshold of 10^{-2} eV/Å between successive relaxation steps. Given that ab initio calculations are computationally expensive, only about 2000–3000 MC attempts (steps) were attempted for each composition. In this study, the "step" refers not to a lattice sweep but rather to every attempted move since obtaining fully relaxed DFT energies is computationally expensive. In the NPT Monte Carlo simulation, two types of moves were possible: the exchange of positions of two different types of metal atoms in the lattice structure, or in the presence of oxygen, the attempted move of an oxygen atom from one interstitial site to another. The Metropolis algorithm was utilized and for each of these possible moves the energy difference and change in volume were calculated by following the proposed move and the move was accepted with a probability of[36]

$$P_{acc} = \min\left[1, \exp\left(N ln\left(\frac{V_2}{V_1}\right) - \beta \Delta U - \beta P \Delta V\right)\right]. \quad (1)$$

In Eq. (1), N is the number of atoms in the system, V_2 is the volume after the attempted move, V_1 is the volume prior to the move, ΔU is the energy difference between the two states, P is the pressure (zero in our case), and $\Delta V = V_2 - V_1$.

After the equilibration run, supercells were sampled from the NPT ensemble at equilibrium and then the thermodynamic behavior of these systems was studied with a Γ-centered $3 \times 3 \times 3$ Monkhorst–Pack grid and an energy cutoff of 450 eV.

RESULTS AND DISCUSSION

Based on the experimental evidence of a single phase disordered bcc structure for the alloy,[37–39] a bcc structure was utilized for the metal in all calculations. MC simulations generated

structures that sampled the isothermal–isobaric ensemble (NPT) with zero pressure and 300 K temperature. When the volumes of these structures were examined, it was found that the average lattice constant was 3.228 Å in agreement with various estimates in the literature for the $Mo_{25}Nb_{25}Ta_{25}W_{25}$ alloy including experimental observations of 3.222 Å[40] and 3.22 Å[37] for first-principles calculations of 3.228 Å[40] and 3.237 Å.[41] Moreover, the alloy mixing enthalpy was calculated to be −0.0999 eV/atom, which was found to be in reasonable agreement with the mixing enthalpy calculated using Calphad by Gao et al.[42] The authors of that study reported an enthalpy of mixing of −0.0902 eV/atom.

After sampling alloy configurations from the NPT ensemble, at least 60 oxygen atom insertions were attempted at random octahedral (O) and another 60 random insertions at tetrahedral (T) interstitial sites. The oxygen solution energy was calculated for each insertion, and the results are displayed in Fig. 1. The oxygen solution energy was calculated using

$$E_s = E(Mo_{14}Nb_{12}Ta_{14}W_{15}\text{-}O) - E(Mo_{14}Nb_{12}Ta_{14}W_{15})$$
$$- \frac{1}{2}E(O_2) . \qquad (2)$$

Figure 1 seems to indicate that both octahedral and tetrahedral sites of the bcc high entropy alloy have comparable energies and this result is consistent with recent experimental observations on another HEA system by Lei et al.[43] who found that interstitial oxygen occupied both octahedral and tetrahedral sites of a bcc high entropy alloy with a similar frequency. Therefore, and in an effort to reduce the computational overhead required for performing the MC simulations in the NPT ensemble, we limited our investigation of the interstitial sites beyond the dilute level to the O-sites only. This is reasonable as the T- and O-sites have comparable energies. Furthermore, it is important to note that for all the oxygen
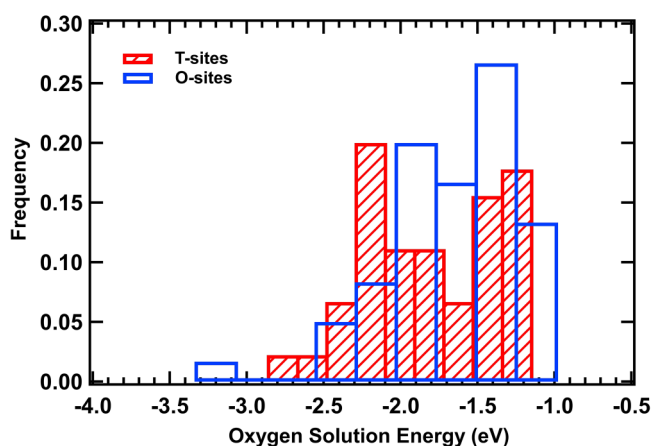

FIG. 1. Oxygen solution energy calculated for inserting a single oxygen atom into different T-sites and O-sites of different the 3 × 3 × 3 bcc metal alloy supercell containing 54 atoms ($Mo_{14}Nd_{12}Ta_{13}W_{15}$) alloy structures sampled from equilibrium using the isothermal–isobaric NPT ensemble at 300 K and zero pressure.

insertions into interstitial sites sampled here the most stable site is actually an O-site.

The dependence of oxygen insertion energy on the local atomic environment was explored by analyzing the energy of each insertion and the chemical composition of the nearest neighboring metallic atoms. This analysis was only conducted for the O sites, and the results are summarized in Figs. 2 and 3. Again, these figures were obtained by first sampling several configurations for the 54-atom $Mo_{14}Nd_{12}Ta_{13}W_{15}$ alloy from the isothermal–isobaric ensemble at 300 K and zero pressure at equilibrium and then inserting a single oxygen atom into random octahedral positions in each of the sampled configurations with the solution energy was computed using Eq. (2).

Figure 2 shows the dependence of the solution energy at the O-site on the composition of the first nearest neighbor metal shell. From Fig. 2(a), it appears that increasing the Mo occupation of the first nearest neighbor shell is associated with decreased stability. The same trend is observed for tungsten as can be seen in Fig. 2(d).

Figure 3 illustrates the dependence of the oxygen solution energy on the composition of the second nearest neighbor (nn) metallic shell. By examining Fig. 3, several trends may be gleaned. From Fig. 3(a), the oxygen solution energy increases (becomes less stable) with the increasing content of Mo in the second nn shell. This trend also holds for tungsten where Fig. 3(d) clearly illustrates a general increase in the oxygen solution energy as the tungsten occupation of the second nn shell increases. Figure 3(b) depicts a general trend where the Nb atoms in the second nn metallic shell have a stabilizing effect on the interstitial oxygen.

Next, structures of the metal alloy supercells containing interstitial oxygen (in the octahedral sites) beyond the dilute level were investigated. To this end, structures of the form $Mo_{14}Nd_{12}Ta_{13}W_{15}\text{-}O_x$ (where x = 3, 5, and 8) were sampled from an isothermal–isobaric ensemble (at 300 K and zero pressure). In the simulation, metal atoms (of different species) were exchanged and oxygen atoms were allowed to sample different octahedral interstitial sites until equilibrium was reached after which a few structures were sampled during a production run. Figure 4 shows that the composition of the nearest neighboring metal atom shells has a dependence on the concentration of interstitial oxygen. When three interstitial oxygen atoms are bound to the O-sites of the 54-atom metal alloy supercell, then the structures sampled from equilibrium favor Ta occupation of the first nearest neighbor shell (relative to the interstitial oxygen atoms) and an overwhelming filling of the second nn shell with Nb atoms. For cases with higher oxygen concentrations (five and eight oxygen atoms bound to O-sites in this study), the structures favor a niobium occupation of both the first and second nearest neighbor metal shells (relative to oxygen) followed by tantalum. Therefore, it is generally clear that all structures favor filling Nb, Ta in the first and second nearest neighbor shells. The results in this figure support recent experimental observations by Butler and Chaput in their analysis of the $Al_{20}Nb_{30}Ta_{10}Ti_{30}Zr_{10}$ refractory complex concentrated alloy (RCCA).[22] The authors of that study found that oxides such as $Ta_2Nb_4O_{15}$ and $NbAlO_4$ formed in the outer composite layer and proposed that such oxides may slow the overall oxidation rate by providing an inherent resistance to the ingress of oxygen.

An additional scrutiny of Fig. 4 reveals that none of the structures sampled from the NPT ensemble favor a tungsten occupation
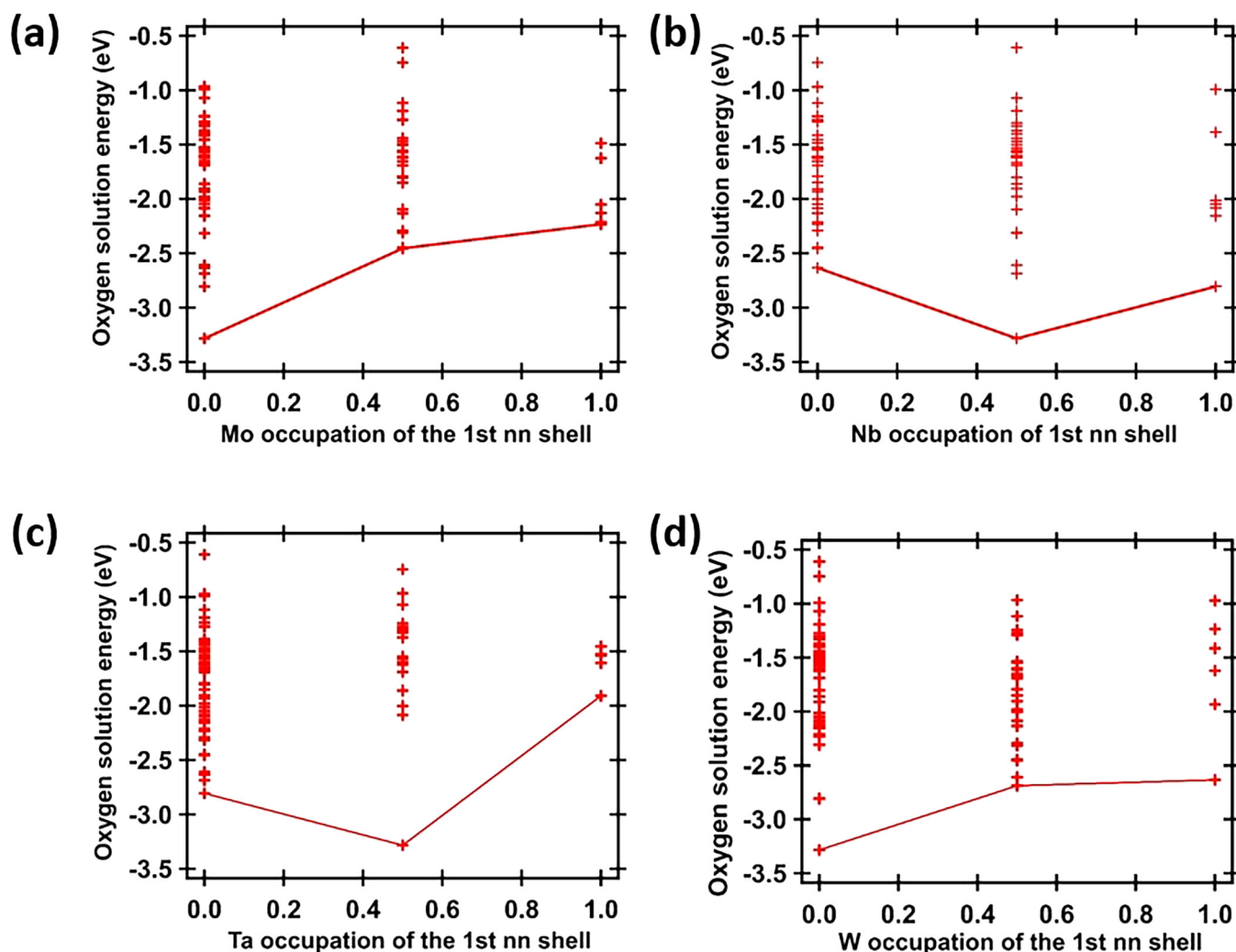
FIG. 2. An examination of the dependence of the oxygen solution energy for a single oxygen at the octahedral interstitial site on the first nearest neighbor metallic shell of the local atomic environment. The lowest energy points are connected by a line to help guide the eyes. (a) shows the Mo occupation of the first nn shell, (b) shows the Nb occupation of the first nn shell, (c) shows the Ta occupation of the first nn shell, and (d) shows the W occupation of the first nn shell.

of the first or second nearest neighbor shells. It is also interesting to note that significant Mo occupation of the first and second nn metallic shells is observed for the case with eight interstitial oxygen atoms (in O-sites).

The sampling of equilibrium configurations beyond the dilute limit of oxygen allows for a deeper understanding of the effects of O–O interactions. To accomplish this, oxygen–oxygen radial distribution functions (RDFs) within the various alloy structures were recorded and analyzed at different oxygen levels and the results are summarized in Fig. 5. These results were calculated by sampling several structures from the isothermal–isobaric ensemble at 300 K, and zero pressure for the structures $Mo_{14}Nb_{12}Ta_{13}W_{15}$-$O_x$ (for $x = 3$, 5, and 8). The results indicate a clustering of the interstitial

oxygen atoms in the alloy with the most likely O–O distance being less than 4 Å in all cases and with this distance decreasing with an increasing number of interstitial oxygen atoms. For three interstitial oxygen atoms, the most likely distance is about 3 Å. This most likely O–O distance increases to about 1.9 Å for five interstitial oxygen atoms in the alloy (with nearly all O–O distances contained in this bin), and finally to about 1.6 Å for eight interstitial O atoms in the alloy. It is clear from examining the RDF plots [particularly Fig. 5(c)] that the oxygen atoms cluster together in an ordered fashion (similar to a solid). This result is consistent with recent experimental observations on oxygen in high entropy alloy systems that have reported on the presence of O-rich clusters in the form of ordered oxygen clusters (OOCs).[43]
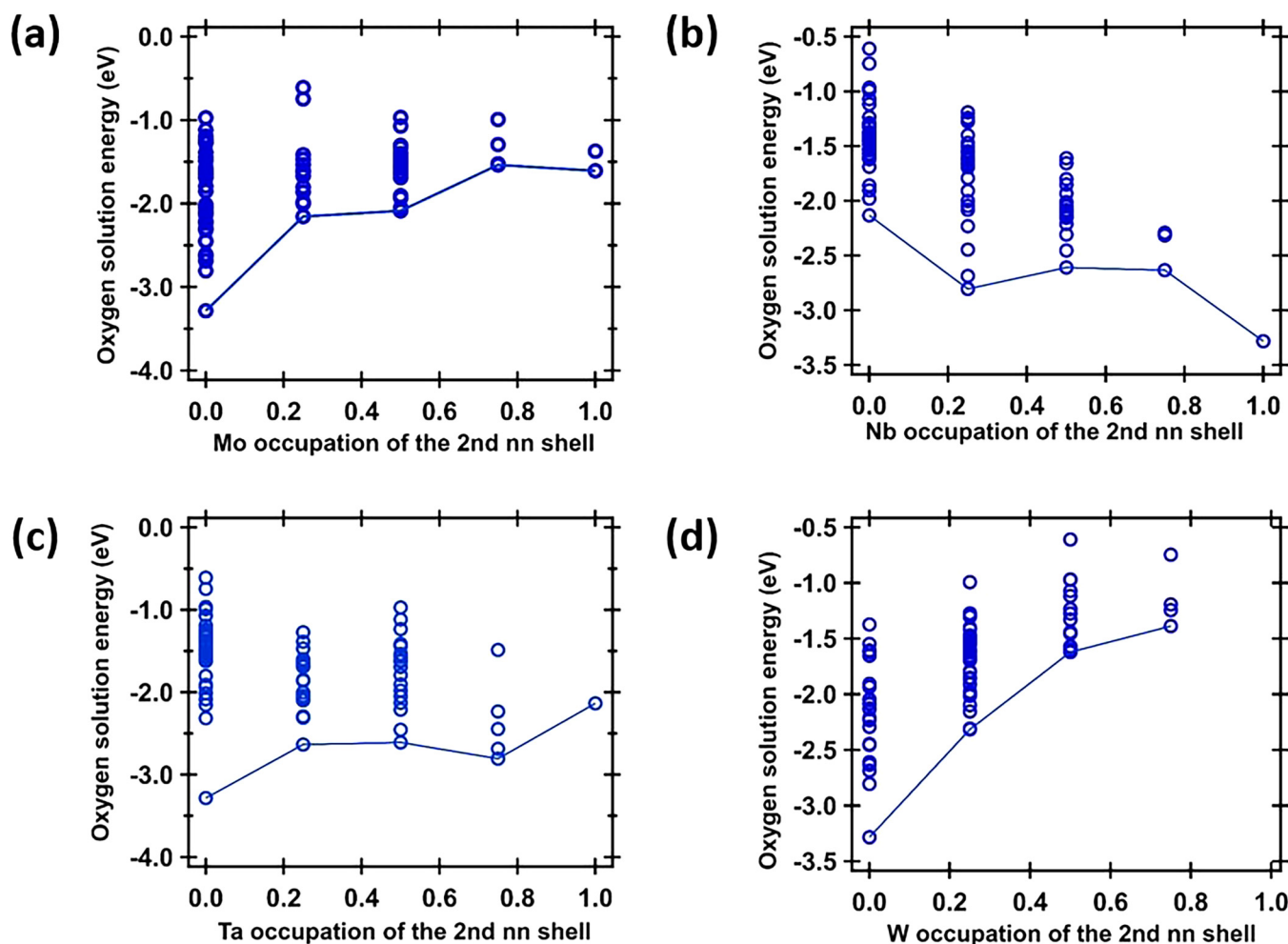
FIG. 3. An examination of the dependence of the oxygen solution energy for a single oxygen at the octahedral interstitial site on the second nearest neighbor metallic shell of the local atomic environment. The lowest energy points are connected by a line to help guide the eyes. (a) shows the Mo occupation of the second nn shell, (b) shows the Nb occupation of the second nn shell, (c) shows the Ta occupation of the second nn shell, and (d) shows the W occupation of the second nn shell.

A visualization of examples of configurations whose RDF plots are shown in Fig. 5 is included in Fig. 6.

Next, the mechanical properties of the alloy were studied to determine the dependence of the elastic constants on the interstitial oxygen concentration. To this end, the mechanical properties of the alloy in the absence of oxygen were determined and compared to the available values in the literature. The results are shown in Table I.

Table I shows that our results for the alloy are consistent with the available theoretical results in the literature. The comparison cannot be exact because the atomic ratios are slightly different in these cases, but our results for the alloy are not too different from the reported calculations in the literature and that matches our expectations. Moreover, the configurational representations for the alloy in our study were found by sampling the isothermal–isobaric ensemble unlike in the study of Hu *et al.*[44] where special quasi-random structures were used. In any case, the mechanical properties of the alloy may be viewed as a reference to explore the effects of gradual interstitial oxidation on the elastic property of the material. To illustrate these effects, the elastic constants were computed for each of the alloys $Mo_{14}Nb_{12}Ta_{13}W_{15}\text{-}O_x$ ($x = 3, 5, 8$) and the results are displayed in Fig. 7. Here, calculations on three configurations sampled from the NPT ensemble (at 300 K and zero pressure) at each O concentration were performed and averaged to determine the elastic constants. It is important to mention that all the calculations of the elastic constants were performed at 0 K using VASP's implementation of IBRION = 6.

Figure 7 clearly reveals a trend where the elastic constants increase with increasing the O-site interstitial oxygen concentration in the alloy. The results show that these elastic constants may increase
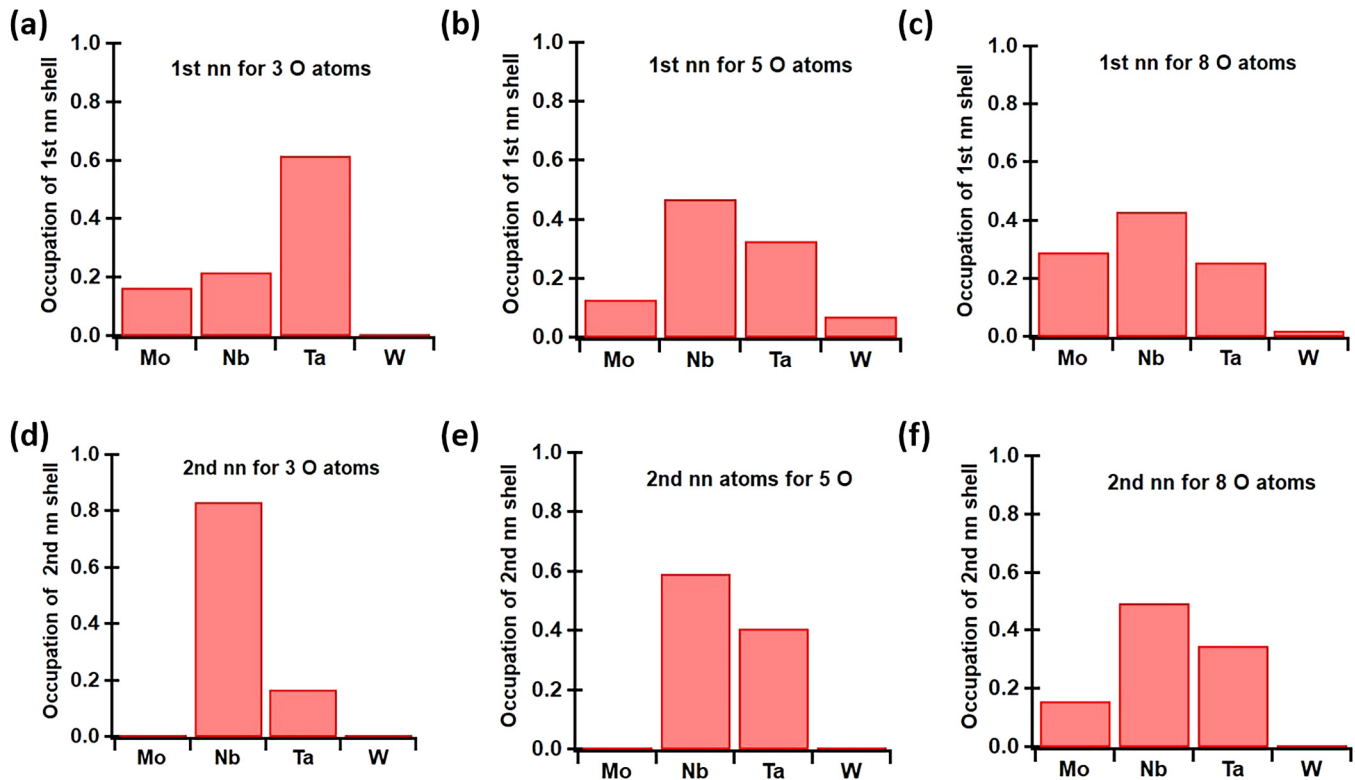
FIG. 4. An analysis of the local atomic environments around oxygen atoms in the octahedral sites for oxygen concentrations beyond the dilute level. The structures analyzed were sampled from equilibrium in the isothermal–isobaric ensemble at 300 K and zero pressure. A series of Monte Carlo NPT simulations were performed on the $3 \times 3 \times 3$ bcc metal alloy supercell containing 54 atoms ($Mo_{14}Nb_{12}Ta_{13}W_{15}$) containing 3 O atoms [(a) and (d)], 5 O atoms [(b) and (e)], and 8 O atoms [(c) and (f)].

by about 8% in value (for the O concentrations used) as a consequence of the interstitial oxygen. Using the calculated elastic constants, the bulk modulus B was found to be 250.47 GPa, 246.65 GPa, 241.28 GPa, and 232.8 GPa for Metal-O_8, Metal-O_5, Metal-O_3, and the oxygen free metal, respectively (where the "metal" stands for $Mo_{14}Nb_{12}Ta_{13}W_{15}$). Clearly, the bulk modulus also increases with increasing concentration of interstitial oxygen atoms. The bulk modulus is a measure of the material's resistance to compression and
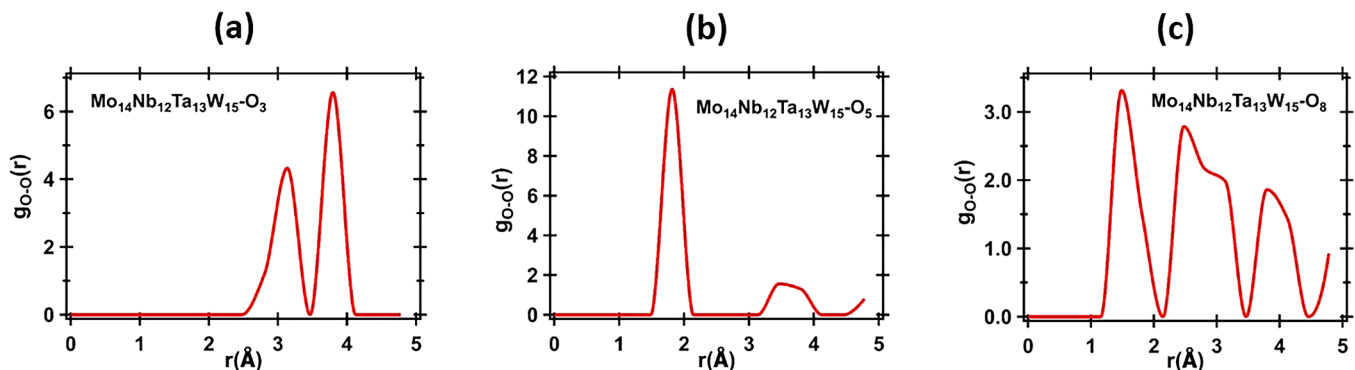
FIG. 5. Radial distribution functions for O–O atoms from metal alloy-oxygen structures sampled at equilibrium for (a) $Mo_{14}Nb_{12}Ta_{13}W_{15}$-$O_3$, (b) $Mo_{14}Nb_{12}Ta_{13}W_{15}$-$O_5$, and (c) $Mo_{14}Nb_{12}Ta_{13}W_{15}$-$O_8$.
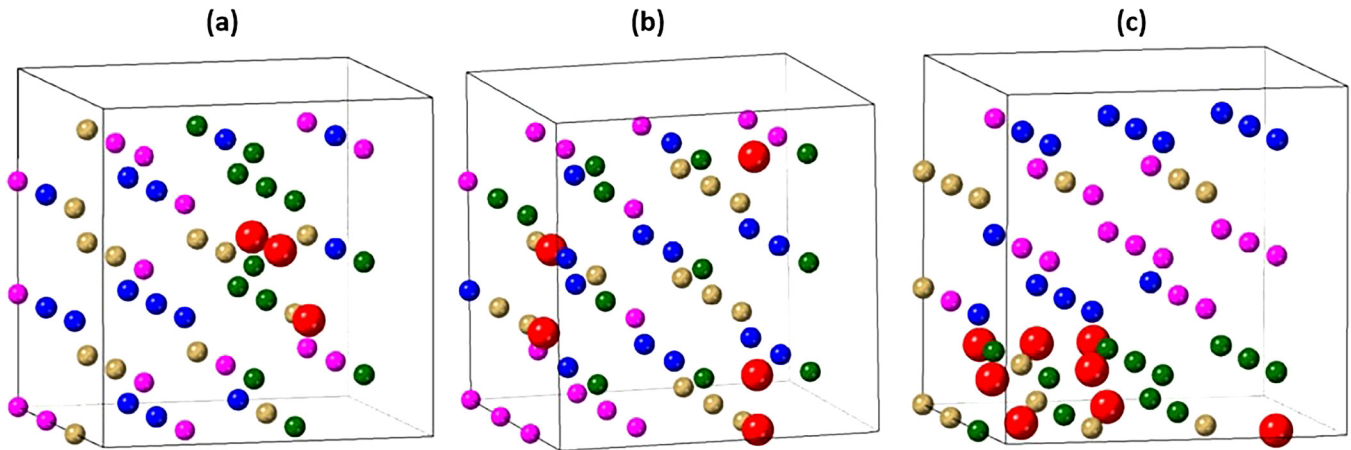
FIG. 6. An illustration of example configurations whose RDF plots are shown in Fig. 5. The contents of exactly one supercell shown. Mo atoms are shown in blue, Nb atoms in green, Ta atoms in brown, W atoms in pink, and O atoms in red. The size of the oxygen atoms relative to the metal atoms is exaggerated to indicate their locations. (a) $Mo_{14}Nb_{12}Ta_{13}W_{15}$-$O_3$, (b) $Mo_{14}Nb_{12}Ta_{13}W_{15}$-$O_5$, and (c) $Mo_{14}Nb_{12}Ta_{13}W_{15}$-$O_8$.

describes the average bond strength between atoms in the material. Our calculations show that the material's resistance to compression becomes enhanced during the early stages of interstitial oxidation. This result is in agreement with recent experimental observations of this phenomenon in other HEA systems.[43,45] For example, Lei *et al.*[43] reported improved strength and ductility in a TiZrHfNb HEA via the formation of ordered interstitial oxygen complexes.

While the results here seem to suggest a slight enhancement of mechanical properties with the addition of a few oxygen atoms, this result may not generalize to all HEAs and it may not be correct to extrapolate such a result to situations containing a higher concentration of oxygen.

Finally, and considering the important role oxygen solubility may play in determining the oxidation thermodynamics of a material and the inward progression of internal oxidation fronts, oxygen solubility in the $Mo_{14}Nb_{12}Ta_{13}W_{15}$ HEA was studied. The solubility of interstitial oxygen in the high entropy alloy as a function of temperature was first calculated in the dilute limit by considering both the O-site solubility and the T-site solubility. In this

calculation, the solubility was predicted by utilizing the binding energies and vibrational frequencies of dissolved oxygen in metals using Eq. (3) through (5),[46]

$$\theta = \frac{1}{K} \cdot \left(\frac{q_{sol}}{\sqrt{\frac{q_{gas}}{PV}} k_B T + q_{sol}} \right), \tag{3}$$

where

$$q_{gas} = \left(\frac{2\pi m_{O_2} k_B T}{h^2} \right)^{\frac{3}{2}} V \frac{8\pi^2 I_{O_2} k_B T}{\sigma h^2} \frac{\exp\left(-\frac{h\nu_{O_2}}{k_B T}\right)}{1 - \exp\left(-\frac{h\nu_{O_2}}{k_B T}\right)} \exp\left(-\frac{E_{O_2}}{k_B T}\right), \tag{4}$$

$$q_{sol} = \prod_{i=1}^{n} \left(\frac{\exp\left(-\frac{h\nu_i}{k_B T}\right)}{1 - \exp\left(-\frac{h\nu_i}{k_B T}\right)} \right) \exp\left(-\frac{E_{ins}}{k_B T}\right). \tag{5}$$

In these equations, m_{O_2} is the mass of the oxygen molecule, and I_{O_2} is moment of inertia, h is Planck's constant, V is the volume (but it cancels out in the calculation), the symmetry number is $\sigma = 2$ for a diatomic molecule (oxygen), and ν_{O_2} and ν_i are the normal mode vibrational frequencies of the oxygen molecule and the atomic oxygen solute in the metal, respectively. E_{O_2} is the electronic energy of the oxygen molecule, and $[E_{ins} = E(\text{Metal} - \text{O}) - E(\text{Metal})]$ is the calculated insertion energy for the interstitial oxygen in the metal. The variable θ in Eq. (3) denotes the solubility as the ratio of the number of dissolved oxygen atoms to the number of metal atoms. The factor (K) takes on the value of

TABLE I. Comparison of the DFT-calculated elastic constants and bulk modulus for the $Mo_{14}Nb_{12}Ta_{13}W_{15}$ alloy with similar theoretical calculations from the literature. Our calculations were performed at 0 K using VASP's implementation of IBRION = 6

	a (Å)	C_{11} (GPa)	C_{44} (GPa)	C_{12} (GPa)	B (GPa)
This work[a]	3.228	383.2	59.6	157.6	232.8
Maresca and Curtin[b41]	3.237	374	64	163	233.3
Hu *et al.*[c44]	3.195	392	79	158	236

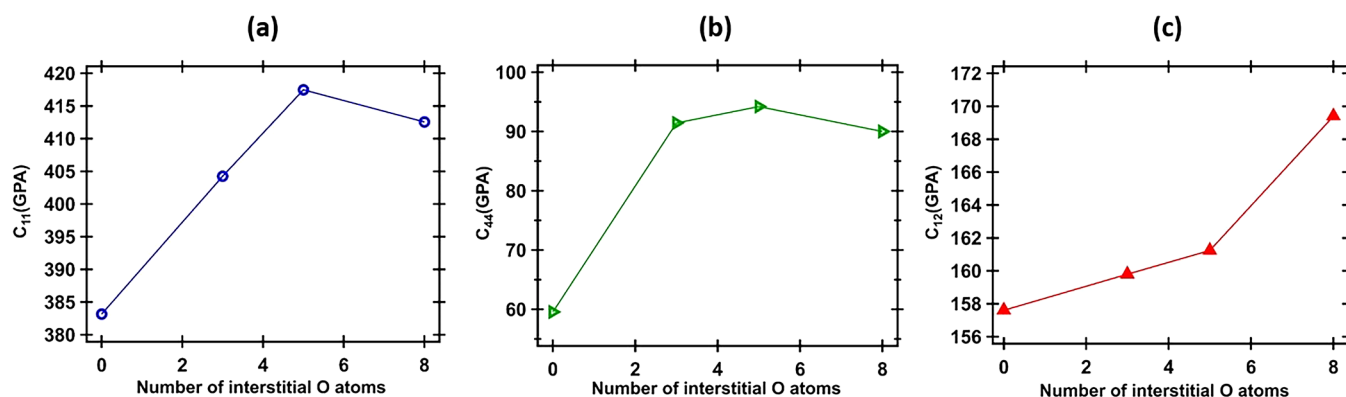[a]$Mo_{14}Nb_{12}Ta_{13}W_{15}$.
[b]$Mo_{25}Nb_{25}Ta_{25}W_{25}$.
[c]MoNbTaW.

FIG. 7. Elastic constants as a function of interstitial oxygen (in the octahedral sites) calculated for $Mo_{14}Nb_{12}Ta_{13}W_{15}$-$O_x$ structures sampled from equilibrium (where $x = 0$, 3, 5, and 8) (a) C_{11}, (b) C_{44}, and (c) C_{12}.

three for octahedral sites and six for tetrahedral sites in a bcc metal. That is because a bcc conventional unit cell contains 2 metal atoms, 6 O-sites, and 12 T-sites. The solubility was calculated at ambient pressure (1 atm = 1.01×10^5 Pa). The DFT calculations for the oxygen molecule were performed by placing an oxygen molecule in a $10 \times 10 \times 10 \, \text{Å}^3$ box and the relaxed distance between the two atoms was found to be 1.23 Å in agreement with the experimental result of 1.21 Å.[47] The vibrational frequency for the oxygen molecule was also calculated to be $1560 \, \text{cm}^{-1}$ consistent with the experimental value of $1556 \, \text{cm}^{-1}$.[48] The normal vibrational frequencies for the atomic oxygen in the metal were calculated by performing 0.005 Å displacements of the oxygen atom only and then taking central finite differences. Both the oxygen solution energy and the vibrational energies were calculated for a number of different sites within different alloy configurations sampled from the NPT ensemble as discussed earlier. These numbers were then averaged, and the results were utilized in Eq. (5). The results of the solubility calculation in the dilute limit are displayed in Fig. 8.

The results in Fig. 8 show that the O-site solubility is almost twice as large as T-site solubility despite the fact that the oxygen solution energies at these sites are comparable. The reason for this can be attributed to the larger number of available T-sites. It is also important to note that these estimates for solubility are only correct in the dilute limit where O–O interactions are not accounted for and this may no longer be valid beyond that regime. Nevertheless, it is interesting to note the behavior of oxygen solubility and that it generally decreases with increasing temperature. Moreover, the T-site and O-site estimates appear to converge for larger temperatures. Figure 8 only examines the oxygen solubility behavior from a thermodynamic point of view but tells us nothing about the kinetics. So while very high oxygen solubility may be thermodynamically favorable at low temperatures, the activation energies to reach such a state may be too large to overcome.

To more accurately examine the solubility beyond the dilute oxygen concentration, we utilized the Widom insertion method.[49] This methodology was used to calculate the chemical potential of the solute using the canonical (NPT) ensemble. The chemical

potential can be expressed as $\mu = \mu_{ideal} + \mu_{excess}$, where

$$\mu_{ideal} = -k_B T \ln\left(\frac{k_B T}{P \, \lambda^3}\right). \tag{6}$$

In Eq. (6), λ is the thermal de-Broglie wavelength of the solute atom, P is the pressure (1.01×10^5 Pa), k_B is the Boltzmann constant, and T is the temperature. The thermal de-Broglie wavelength
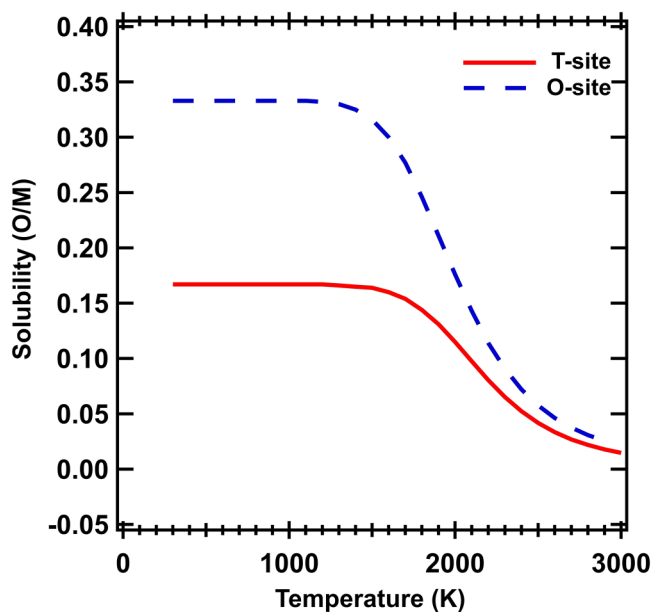

FIG. 8. Solubility for oxygen in $Mo_{14}Nb_{12}Ta_{13}W_{15}$ calculated in the dilute limit for oxygen occupying both the tetrahedral (T-sites) and the octahedral sites (O-sites) as a function of temperature.

may be obtained via

$$\lambda = \sqrt{\frac{2\pi\hbar^2}{mk_BT}}, \tag{7}$$

where m is the mass of the solute atom (oxygen). The excess chemical potential may be calculated by an NPT ensemble average over the N particle system, which is denoted by the angular brackets as shown in

$$\mu_{excess} = -k_BT\ln\left(\frac{\left\langle V\exp\left(-\frac{\Delta U}{k_BT}\right)\right\rangle}{\langle V\rangle}\right), \tag{8}$$

where the insertion energy given by $\Delta U = E(Metal - O_{x+1}) - E(Metal - O_x)$ is the change of energy following the random insertion of an oxygen atom and its interaction with the rest of the system. The angular brackets denote ensemble averaging over all positions of the inserted atom (where the structure before the insertion is sampled from the NPT ensemble). The solubility of the solute corresponds to the fraction of atoms that yields the same chemical potential as the free gas, i.e.,

$$\mu(\text{oxygen; metal}) = \frac{1}{2}\mu(O_2). \tag{9}$$

Moreover, the binding energy was evaluated using

$$E_{bind} = E(Metal - O_{x+1}) - E(Metal - O_x) - \frac{1}{2}E(O_2). \tag{10}$$

The solution energy and the binding energy are equivalent within the context of this paper. These energies are a function of the amount of oxygen in the metal. The insertion energy is different from the binding (solution) energy as it measures the excess energy from adding one oxygen atom to the system. The binding energies were calculated for all the random insertions into octahedral sites of structures of the form $Mo_{14}Nb_{12}Ta_{13}W_{15}$-$O_x$ (with $x = 0$, 3, 5, and 8) sampled from the NPT ensemble. The results are included in Fig. 9(a) and it can be clearly seen that the binding energy for the vast majority of attempted insertions into octahedral sites in the metal is attractive. This is consistent with the calculated radial distribution functions in Fig. 5 and the experimentally observed clustering of interstitial oxygen in high entropy alloys.[43] Figure 9(b) shows the final volume of the system after insertion when the termination criteria for the DFT calculations (atomic and volumetric relaxation) have been met. The figure appears to be levelling off as the number of oxygen atoms increases in the system. This observation also supports the notion of attractive O–O interactions and clustering within the system.

The solubility of interstitial oxygen in the metal system was then examined through the Widom insertion method to account for the O–O interactions which clearly are significant and cannot be ignored. Using the calculated values for the insertion energy and the final volume after each insertion, the results for the solute oxygen chemical potential in the metal and the oxygen chemical potential in gas were plotted for different temperatures and recorded in Fig. 9. The chemical potential for the oxygen gas was calculated by using[46]

$$\mu_{O_2,\,gas} = -k_BT\ln\left(\frac{q_{gas}}{PV}k_BT\right). \tag{11}$$

(a)

(b)

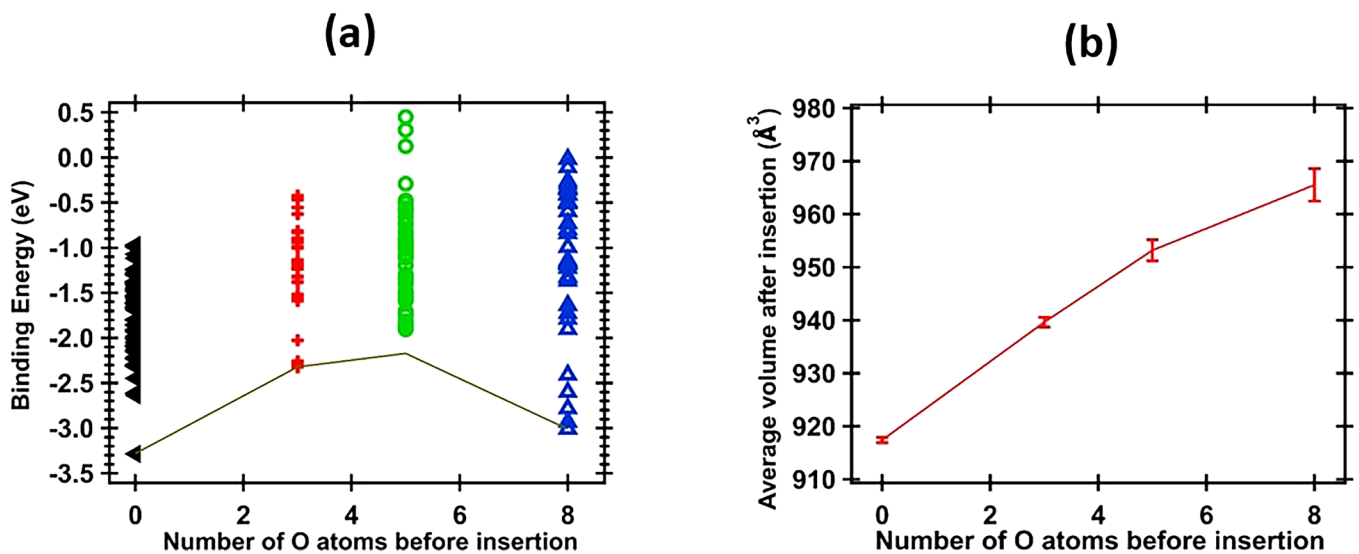**FIG. 9.** (a) The binding energy of one oxygen into $Mo_{14}Nb_{12}Ta_{13}W_{15}$-$O_x$ structures sampled from equilibrium (where $x = 0$, 3, 5, and 8) with oxygen occupying the octahedral sites. (b) The volume of the supercell after O insertion as a function of the number of oxygen atoms originally contained in the structure before insertion. The average volume of the clean metal alloy not containing any oxygen was 907.86 Å^3.

The chemical potential for the oxygen in the gaseous form in Fig. 10 was obtained by Eq. (11) (multiplied by ½) as required by Eq. (9).

In obtaining the results of Fig. 10, the vibrational contribution to the insertion energy was approximated by utilizing the vibrational frequencies calculated for the single interstitial atom in the O-site to calculate the zero point energy correction. This same zero point energy calculated for the case of one oxygen interstitial atom in the structure was used for all structures. While this is not exact, it does allow us to approximately account for the vibrational effects to a degree and these effects become important as the temperature increases. Figure 10(b) shows an enlargement of a small section of Fig. 10(a) to more clearly illustrate the behavior of the chemical potential of the oxygen atom solute in the metal at different temperatures.

Upon examination of Fig. 10(a), we see that the chemical potentials for all the concentrations considered here (up to 0.167 atomic fraction) are below the chemical potential of the oxygen gas evaluated at 300 K. This means that the solubility of oxygen at 300 K must be greater than 0.167 (O/M). This conclusion is in agreement with the dilute formula treatment, which essentially predicts the solubility at 300 K to be between 0.17 and 0.34 (O/M). Figure 10(b) also shows that the solubility of oxygen at 600 K is also greater than 0.17 (O/M). Furthermore, the particle insertion method also predicts that solubility decreases with increasing temperature. For example, Fig. 9(b) shows the point at which the two plots cross for temperature 1000 K corresponding to an atomic fraction of about 0.05 O/M. This trend is also consistent with the solubility behavior as a function of temperature calculated in the dilute limit. However, in the dilute limit at 1000 K, the solubility is predicted to be larger (still between 0.17 and 0.34 O/M). The solubility limit is exceeded for

all the concentrations shown for the cases of 1500 K and 2000 K meaning that it is expected that the solubility is lower than 0.02 atomic fraction for these temperatures. Again, it should be emphasized that these plots tell us nothing about the kinetics of the process and how fast the oxygen dissolves in the alloy.

Another interesting observation to be made here is that the Widom particle insertion method appears to be showing a departure from the monotone decreasing trend displayed by the solubility lines in the dilute limit. This is especially obvious when we notice that the chemical potential first increases for low concentrations but then starts decreasing again at higher concentrations (9/54 atomic fraction). This is due to the attractive nature of the interactions between the oxygen atoms, which tend to cluster together at higher concentrations. This attractive interaction indicates that some departure from the dilute limit predictions can be expected for higher concentrations of oxygen.

It is important to note the limitation of this analysis. Only octahedral interstitial sites were considered here and the important role that substitutional defects, vacancies, and grain boundaries may play in real experiments has been completely ignored. Another limitation of the current study was the computationally expensive nature of the DFT-based NPT simulation. Due to this computational overhead, it was only possible to perform 2000–3000 MC steps per configuration. Roughly 75% of these steps were considered the equilibration part of the run and sampling was performed over the final 25% of the trajectory (the production run). Therefore, it is possible that a true equilibrium may not have been achieved. In the present study, the vibrational contribution to the total energy within the NPT Monte Carlo simulations was completely ignored. Furthermore, and within the current implementation of the Widom particle insertion method, the vibrational
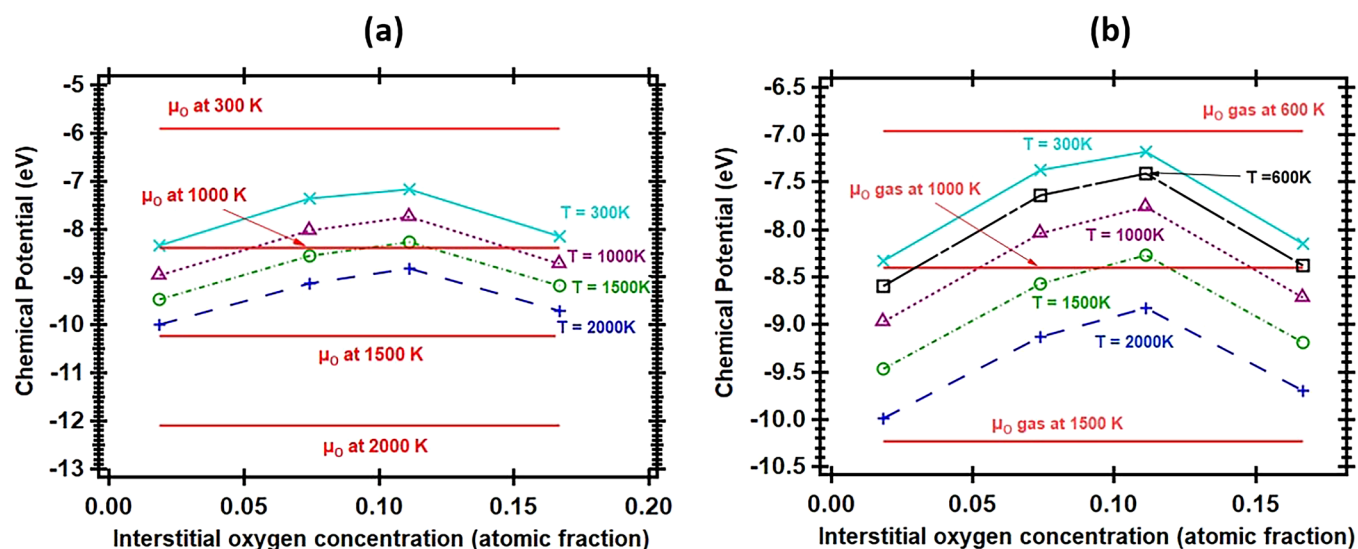
FIG. 10. (a) The chemical potential for the oxygen atom in gas form at different temperatures (red lines) and the chemical potential for an interstitial oxygen atom inserted into $Mo_{14}Nb_{12}Ta_{13}W_{15}$-$O_x$ structures sampled from equilibrium at 300 K and zero pressure (where $x = 0$, 3, 5, and 8) with oxygen occupying the octahedral sites. (b) depicts an enlarged section of (a) for more clarity.

contribution to the oxygen insertion energy was approximate and based on the zero point energy correction calculated for a single interstitial oxygen in the structure. It is also important to stress that the sampling of the NPT ensemble was only done at 300 K.

CONCLUSIONS

In this work, the thermodynamic behavior of interstitial oxygen in an Mo-Nb-Ta-W HEA was studied via first-principles calculations. The analysis accounted for oxygen–oxygen interactions and considered concentrations beyond the dilute limit. A series of Mo-Nb-Ta-W-O_x (for $x = 0, 3, 5, 8$) were sampled from an isothermal–isobaric ensemble at zero pressure and 300 K. Zero pressure was selected to allow for atomic and structural relaxation in the DFT calculations. When a single oxygen atom was inserted into HEA configurations sampled from the NPT ensemble, it was found that O-sites and T-sites had comparable stability consistent with recent experimental observations. This led us to limit our analysis to O-sites for calculations beyond the dilute limit. The Mo-Nb-Ta-W-O_x structures sampled from equilibrium showed that the O-site interstitial oxygen atoms favored Nb and Ta to occupy the first and second nearest neighbor metal shell surrounding the oxygen. An analysis of the O–O RDF plots from the equilibrated structures showed that oxygen atoms clustered together in an ordered fashion. Furthermore, it was found that random insertions of additional oxygen atoms into the equilibrated structures led to overwhelmingly negative binding energies indicating attractive interactions. It was additionally found that the interstitial O-site oxygen may enhance the mechanical properties of the alloy through the ordered structures. The solubility of oxygen in the alloy was also examined using two different methods. The first approach following Lee et al.[46] in the dilute limit led to a solubility of (0.17–0.34) atomic fraction at 300 K. This approach agreed with the solubility calculated using the Widom insertion technique. Both methods led to decreased solubility with increasing oxygen concentration. The kinetics of oxidation, the roles of vacancies, and grain boundaries were also ignored in this study.

ACKNOWLEDGMENTS

DATA AVAILABILITY

The data that support the findings of this study are available from the corresponding author upon reasonable request.

REFERENCES

[1]J.-W. Yeh, S.-K. Chen, S.-J. Lin, J.-Y. Gan, T.-S. Chin, T.-T. Shun, C.-H. Tsau, and S.-Y. Chang, "Nanostructured high-entropy alloys with multiple principal elements: Novel alloy design concepts and outcomes," Adv. Eng. Mater. **6**, 299–303 (2004).

[2]B. Cantor, I. T. H. Chang, P. Knight, and A. J. B. Vincent, "Microstructural development in equiatomic multicomponent alloys," Mater. Sci. Eng. A **375–377**, 213–218 (2004). .

[3]D. B. Miracle, "High entropy alloys as a bold step forward in alloy development," Nat. Commun. **10**, 1805 (2019).

[4]K. R. Lim, K. S. Lee, J. S. Lee, J. Y. Kim, H. J. Chang, and Y. S. Na, "Dual-phase high-entropy alloys for high-temperature structural applications," J. Alloys Compd. **728**, 1235–1238 (2017).

[5]H. Shi, C. Tang, A. Jianu, R. Fetzer, A. Weisenburger, M. Steinbrueck, M. Grosse, R. Stieglitz, and G. Müller, "Oxidation behavior and microstructure evolution of alumina-forming austenitic & high entropy alloys in steam environment at 1200 °C," Corros. Sci. **170**, 108654 (2020).

[6]M. Elbakhshwan, W. Doniger, C. Falconer, M. Moorehead, C. Parkin, C. Zhang, K. Sridharan, and A. Couet, "Corrosion and thermal stability of CrMnFeNi high entropy alloy in molten FLiBe salt," Sci. Rep. **9**, 1–10 (2019).

[7]O. A. Waseem, J. Lee, H. M. Lee, and H. J. Ryu, "The effect of Ti on the sintering and mechanical properties of refractory high-entropy alloy TixWTaVCr fabricated via spark plasma sintering for fusion plasma-facing materials," Mater. Chem. Phys. **210**, 87–94 (2018).

[8]Y. Tong, D. Chen, B. Han, J. Wang, R. Feng, T. Yang, C. Zhao, Y. L. Zhao, W. Guo, Y. Shimizu, C. T. Liu, P. K. Liaw, K. Inoue, Y. Nagai, A. Hu, and J. J. Kai, "Outstanding tensile properties of a precipitation-strengthened FeCoNiCrTi0.2 high-entropy alloy at room and cryogenic temperatures," Acta Mater. **165**, 228–240 (2019).

[9]W. Fu, W. Zheng, Y. Huang, F. Guo, S. Jiang, P. Xue, Y. Ren, H. Fan, Z. Ning, and J. Sun, "Cryogenic mechanical behaviors of CrMnFeCoNi high-entropy alloy," Mater. Sci. Eng. A **789**, 139579 (2020).

[10]Y. Lu, H. Huang, X. Gao, C. Ren, J. Gao, H. Zhang, S. Zheng, Q. Jin, Y. Zhao, C. Lu, T. Wang, and T. Li, "A promising new class of irradiation tolerant materials: Ti2ZrHfV0.5Mo0.2 high-entropy alloy," J. Mater. Sci. Technol. **35**, 369–373 (2019).

[11]O. El-Atwani, N. Li, M. Li, A. Devaraj, J. K. S. Baldwin, M. M. Schneider, D. Sobieraj, J. S. Wróbel, D. Nguyen-Manh, S. A. Maloy, and E. Martinez, "Outstanding radiation resistance of tungsten-based high-entropy alloys," Sci. Adv. **5**, eaav2002 (2019).

[12]B. Gorr, F. Müller, M. Azim, H.-J. Christ, T. Müller, H. Chen, A. Kauffmann, and M. Heilmaier, "High-Temperature oxidation behavior of refractory high-entropy alloys: Effect of alloy composition," Oxid. Met. **88**, 339–349 (2017).

[13]T. M. Butler, K. J. Chaput, J. R. Dietrich, and O. N. Senkov, "High temperature oxidation behaviors of equimolar NbTiZrV and NbTiZrCr refractory complex concentrated alloys (RCCAs)," J. Alloys Compd. **729**, 1004–1019 (2017).

[14]T. Li, O. J. Swanson, G. S. Frankel, A. Y. Gerard, P. Lu, J. E. Saal, and J. R. Scully, "Localized corrosion behavior of a single-phase non-equimolar high entropy alloy," Electrochim. Acta **306**, 71–84 (2019).

[15]H. Torbati-Sarraf, M. Shabani, P. D. Jablonski, G. J. Pataky, and A. Poursaee, "The influence of incorporation of Mn on the pitting corrosion performance of CrFeCoNi high entropy alloy at different temperatures," Mater. Des. **184**, 108170 (2019).

[16]N. Kumar, M. Fusco, M. Komarasamy, R. S. Mishra, M. Bourham, and K. L. Murty, "Understanding effect of 3.5 wt.% NaCl on the corrosion of Al0.1CoCrFeNi high-entropy alloy," J. Nucl. Mater. **495**, 154–163 (2017).

[17]G. Brewster, I. M. Edmonds, and S. Gray, "The effect of volatilisation of refractory metal oxides on the cyclic oxidation of Ni-base superalloys," Oxid. Met. **81**, 345–356 (2014).

[18]F. Koch, S. Köppl, and H. Bolt, "Self passivating W-based alloys as plasma-facing material," J. Nucl. Mater. **386-388**, 572–574 (2009).

[19]F. Müller, B. Gorr, H. J. Christ, J. Müller, B. Butz, H. Chen, A. Kauffmann, and M. Heilmaier, "On the oxidation mechanism of refractory high entropy alloys," Corros. Sci. **159**, 108161 (2019).

[20]X. Zhang, D. Li, Y. Li, and S. Lu, "Oxidation behaviors of Fe-25Cr-20Ni-χNb austenitic weld metals at 1100 °C in ambient air: Role of elemental niobium," Corros. Sci. **159**, 108137 (2019).

[21]J. Jayaraj, P. Thirathipviwat, J. Han, and A. Gebert, "Microstructure, mechanical and thermal oxidation behavior of AlNbTiZr high entropy alloy," Intermetallics **100**, 9–19 (2018).

[22]T. M. Butler and K. J. Chaput, "Native oxidation resistance of Al20Nb30Ta10Ti30Zr10 refractory complex concentrated alloy (RCCA)," J. Alloys Compd. **787**, 606–617 (2019).

[23]C. M. Liu, H. M. Wang, S. Q. Zhang, H. B. Tang, and A. L. Zhang, "Microstructure and oxidation behavior of new refractory high entropy alloys," J. Alloys Compd. **583**, 162–169 (2014).

[24]Y. Hong, M. Beyramali Kivy, and M. Asle Zaeem, "Competition between formation of Al2O3 and Cr2O3 in oxidation of Al0.3CoCrCuFeNi high entropy alloy: A first-principles study," Scr. Mater. **168**, 139–143 (2019).

[25]E. Osei-Agyemang and G. Balasubramanian, "Surface oxidation mechanism of a refractory high-entropy alloy," Npj Mater. Degrad. **3**, 1–8 (2019).

[26]A. Ferrari and F. Körmann, "Surface segregation in Cr-Mn-Fe-Co-Ni high entropy alloys," Appl. Surf. Sci. **533**, 147471 (2020).

[27]P. E. Blöchl, "Projector augmented-wave method," Phys. Rev. B **50**, 17953–17979 (1994).

[28]G. Kresse and D. Joubert, "From ultrasoft pseudopotentials to the projector augmented-wave method," Phys. Rev. B **59**, 1758–1775 (1999).

[29]G. Kresse and J. Furthmüller, "Efficiency of ab-initio total energy calculations for metals and semiconductors using a plane-wave basis set," Comput. Mater. Sci. **6**, 15–50 (1996).

[30]G. Kresse and J. Furthmüller, "Efficient iterative schemes for ab initio total-energy calculations using a plane-wave basis set," Phys. Rev. B **54**, 11169–11186 (1996).

[31]M. C. Payne, M. P. Teter, D. C. Allan, T. A. Arias, and J. D. Joannopoulos, "Iterative minimization techniques for ab initio total-energy calculations: Molecular dynamics and conjugate gradients," Rev. Mod. Phys. **64**, 1045–1097 (1992).

[32]J. P. Perdew, K. Burke, and M. Ernzerhof, "Generalized gradient approximation made simple," Phys. Rev. Lett. **77**, 3865–3868 (1996).

[33]G. Kresse, see https://www.vasp.at/vasp-workshop/pseudoppdatabase.pdf for The PAW and US-PP database; accessed 9 March 2020.

[34]M. Methfessel and A. T. Paxton, "High-precision sampling for Brillouin-zone integration in metals," Phys. Rev. B **40**, 3616–3621 (1989).

[35]H. J. Monkhorst and J. D. Pack, "Special points for Brillouin-zone integrations," Phys. Rev. B **13**, 5188–5192 (1976).

[36]M. E. Tuckerman, *Statistical Mechanics: Theory and Molecular Simulation*, 1st ed. (Oxford University Press, 2010).

[37]O. N. Senkov, G. B. Wilks, J. M. Scott, and D. B. Miracle, "Mechanical properties of Nb25Mo25Ta25W25 and V20Nb20Mo20Ta20W20 refractory high entropy alloys," Intermetallics **19**, 698–706 (2011).

[38]M. Moorehead, K. Bertsch, M. Niezgoda, C. Parkin, M. Elbakhshwan, K. Sridharan, C. Zhang, D. Thoma, and A. Couet, "High-throughput synthesis of Mo-Nb-Ta-W high-entropy alloys via additive manufacturing," Mater. Des. **187**, 108358 (2020).

[39]Y. Tong, P. Qi, X. Liang, Y. Chen, Y. Hu, and Z. Hu, "Different-shaped ultra-fine MoNbTaW HEA powders prepared via mechanical alloying," Materials **11**, 1250 (2018).

[40]Y. Zou, S. Maiti, W. Steurer, and R. Spolenak, "Size-dependent plasticity in an Nb25Mo25Ta 25W25 refractory high-entropy alloy," Acta Mater. **65**, 85–97 (2014).

[41]F. Maresca and W. A. Curtin, "Mechanistic origin of high strength in refractory BCC high entropy alloys up to 1900K," Acta Mater. **182**, 235–249 (2020).

[42]M. C. Gao, C. S. Carney, N. Doğan, P. D. Jablonksi, J. A. Hawk, and D. E. Alman, "Design of refractory high-entropy alloys," JOM **67**, 2653–2669 (2015).

[43]Z. Lei, X. Liu, Y. Wu, H. Wang, S. Jiang, S. Wang, X. Hui, Y. Wu, B. Gault, P. Kontis, D. Raabe, L. Gu, Q. Zhang, H. Chen, H. Wang, J. Liu, K. An, Q. Zeng, T. G. Nieh, and Z. Lu, "Enhanced strength and ductility in a high-entropy alloy via ordered oxygen complexes," Nature **563**, 546–550 (2018).

[44]Y. L. Hu, L. H. Bai, Y. G. Tong, D. Y. Deng, X. B. Liang, J. Zhang, Y. J. Li, and Y. X. Chen, "First-principle calculation investigation of NbMoTaW based refractory high entropy alloys," J. Alloys Compd. **827**, 153963 (2020).

[45]Y. Chen, Y. Li, X. Cheng, Z. Xu, C. Wu, B. Cheng, and M. Wang, "Interstitial strengthening of refractory ZrTiHfNb0.5Ta0.5Ox (x = 0.05, 0.1, 0.2) high-entropy alloys," Mater. Lett. **228**, 145–147 (2018).

[46]K. Lee, M. Yuan, and J. Wilcox, "Understanding deviations in hydrogen solubility predictions in transition metals through first-principles calculations," J. Phys. Chem. C **119**, 19642–19653 (2015).

[47]W. M. Haynes, D. R. Lide, and T. J. Bruno, *CRC Handbook of Chemistry and Physics: A Ready-Reference Book of Chemical and Physical Data* (CRC Press, 2017), see http://public.eblib.com/choice/publicfullrecord.aspx?p=4711508.

[48]K. P. Huber and G. Herzberg, *Molecular Spectra and Molecular Structure* (Springer, 1979).doi:10.1007/978-1-4757-0961-2.

[49]B. Widom, "Some topics in the theory of fluids," J. Chem. Phys. **39**, 2808–2812 (1963).